Photo-electrochemical properties of $CuO–TiO_2$ heterojunctions for glucose sensing

David Maria Tobaldi,[a*] Claudia Espro,[b] Salvatore Gianluca Leonardi,[b] L Lajaunie,[c,d] Maria Paula Seabra,[a] JJ Calvino,[c,d] Silvia Marini,[b] João António Labrincha,[a] Giovanni Neri[b*]

[a] *Department of Materials and Ceramics Engineering and CICECO–Aveiro Institute of Materials – University of Aveiro, 3810–193 Campus Universitário de Santiago, Portugal*

[b] *Department of Engineering, University of Messina, C.da Di Dio, I–98166 Messina, Italy*

[c] *Departamento de Ciencia de los Materiales e Ingeniería Metalúrgica y Química Inorgánica, Facultad de Ciencias, Universidad de Cádiz, Campus Río San Pedro S/N, Puerto Real 11510, Cádiz, Spain*

[d] *Instituto Universitario de Investigación de Microscopía Electrónica y Materiales (IMEYMAT), Facultad de Ciencias, Universidad de Cádiz, Campus Río San Pedro S/N, Puerto Real 11510, Cádiz, Spain*

KEYWORDS: Non-enzymatic electrochemical sensors; Photochemical activation; glucose; $Cu_xO–TiO_2$ junction

***Corresponding authors**

E-mail addresses: david.tobaldi@ua.pt; david@davidtobaldi.org (DM Tobaldi); gneri@unime.it (G Neri).

Twitter: @D14MT (DM Tobaldi)

Abstract

Electrochemical sensors for monitoring biochemical substances are attracting considerable attention. These devices are usually based on enzymes that are sensitive and very specific. Still, the activity of those enzymes is lost with changes in temperature or pH. Non-enzymatic electrochemical sensors – fabricated *via* the modification of the electrode surface with metal oxide nanoparticles – are a judicious answer. In this study, we investigated the photo-electrochemical properties of CuO–TiO_2 heterojunctions for glucose sensing in alkaline media. A combination of high-resolution (scanning) transmission electron microscopy, spatially resolved electron energy-loss spectroscopy, energy-dispersive X-ray spectroscopy and X-ray powder diffraction, was used to study in detail the microstructures of the prepared specimens. These results highlighted the strong intertwining between the TiO_2 nanoparticles and the Cu-based nanoparticles, which present a metallic core with a CuO rich surface. In addition, we showed that CuO, joint to TiO_2, has smaller size compared to pure CuO, which entails larger surface area available for the glucose electro-oxidation, which consequently enhanced the electrochemical features. The influence of Cu loading over the sensing performance of TiO_2 was examined in detail carrying out electrochemical sensing tests under dark, laboratory illumination and halogen lamp irradiation. Results demonstrated that, under halogen lamp irradiation, the modified CuO–TiO_2 electrodes showed a higher specific response signal than that of pure CuO. Those increased photo-electrochemical properties in CuO–TiO_2 heterojunctions are likely due to a synergistic effect between the microstructural characteristics and effective separation of photo-generated exciton created at the heterojunction interface. Results of this study offer applicable guidelines for designing photo-electrochemical screen-printed electrodes based on nano-sized CuO on titania for an efficient detection of glucose.

1 INTRODUCTION

The development of new electrochemical sensors for monitoring biochemical substances is a very competitive research area and, as such, has high relevance and applications in industrial, pharmaceutical, food and personal care fields. Today, these devices are generally based on enzymes that are sensitive and very specific [1]. For instance, cholesterol, glucose and triglyceride are usually determined *via* the quantitation of hydrogen peroxide production in enzymatic or enzymatic-like reactions [2]. However, the activity of enzymes is affected by instability, high cost of enzymes, complicated immobilisation procedures and critical operating conditions [3]. Non-enzymatic electrochemical sensors have become of great interest through the modification of the electrode surface with metal oxide nanoparticles (NPs) [4]. For example, metals oxides, such as copper oxide (CuO) and nickel oxide (NiO), are often recognised to be viable solutions for the oxidation of glucose [5], which allows for glucose to be directly oxidised on the electrode surface [6–8]. These researches shall provide a development in high sensitive, robust and precise non-enzymatic electrochemical sensors for the quantification of glucose in clinical, pharmaceutical and industrial sectors. Indeed, because of their broad applications, particularly in diabetes diagnosis, the research about glucose sensors is extensive nowadays [9]. Diabetes has become one of the most common diseases worldwide, with a death-toll of around 1.6 million in 2016 [10]. As accurate detection of human glucose concentration is an effective way to prevent or treat diabetes, a cheap, affordable yet effective fabrication of glucose monitoring devices is imperative [11].

Given this context, here we present a study devoted to the optimisation of the photo-electrochemical properties towards glucose oxidation of CuO NPs on titanium dioxide (TiO_2). CuO NPs received considerable interest due to their high activity towards glucose oxidation in alkaline conditions, whereas TiO_2 NPs possess many advantages, *i.e.* large surface area, excellent semiconducting properties, low-cost, high chemical stability. Besides, they are very well known to exhibit photo-catalytic properties in the oxidation of various organic molecules [12]. CuO–TiO_2 heterojunctions have been widely used as composite photocatalyst to decrease the recombination of the photo-generated exciton, as well as to increase reaction kinetics, whereby charge carriers are transferred along junctions formed at the interface between the semiconductor particles [13]. Thus, we synthesised CuO–TiO_2 heterojunctions with different CuO loadings with the aim to investigate that system for glucose sensing.

Photo-activated electrochemical (PEC) sensors based on photocatalytic systems have been recently exploited for electroanalytical purposes, attracting great attention for obtaining high sensitivity with low background noise [14]. Most of these systems are based on TiO_2, a semiconductor material which has received significant attention for various applications such as gas sensors, solar cells,

water splitting and, more recently, for the development of electrochemical sensors [15,16]. On the other hand, copper oxides have been already reported for PEC sensing of some biomolecules under visible-light irradiation [17,18]. It is also well-known that CuO contributes as visible-light absorber in CuO–TiO_2 photocatalytic systems [19,20].

Despite glucose sensing being of outmost importance, studies on CuO–TiO_2 composites for the electrochemical sensing of glucose are surprisingly very much limited [21–24]. Furthermore, and even more surprising, in the wide body of literature on photocatalysis, studies on CuO–TiO_2 heterojunctions for PEC sensing of glucose are totally lacking.

Out on these bases, CuO–TiO_2 screen-printed carbon electrodes (SPCE) have been fabricated and tested under dark condition, laboratory, and halogen lamp irradiation. The objective was to investigate the PEC performances of CuO–TiO_2 heterojunctions for an efficient quantification of glucose.

2 EXPERIMENTAL

2.1 CuO–TiO_2 synthesis

Aqueous titanium(IV) hydroxide sols were made *via* the carefully controlled hydrolysis and peptization of titanium(IV) isopropoxide (Ti-i-pr, $Ti(OCH\text{-}(CH_3)_2)_4$) with distilled water diluted in isopropyl alcohol (IPA, propan-2-ol), following a protocol previously reported in detail [25]. CuO modified TiO_2 sols, with a TiO_2:CuO molar ratios ranging between 1.0:0.0 to 0.0:1.0, were prepared adding stoichiometric amounts of copper(II) nitrate trihydrate (Aldrich, ≥ 98.5%) to the TiO_2 sol Afterwards, dried gels were thermally treated at 450 °C under a static air flow, at heating/cooling rate of 5 °C.min^{-1}. CuO end-member (*i.e.* TiO_2:CuO molar ratio equal to 0.0:1.0) was similarly prepared and thermally treated at the same temperature.

2. 2 Samples characterisation

Analysis using X-ray powder diffraction (XRPD) was carried out to quantify the weight percentage of crystalline phases in the specimens prepared in addition to microstructural features. Semi-quantitative phase analysis (QPA) of the XRPD data was performed using the Rietveld method. Rietveld refinements were assessed using the GSAS-EXPGUI software suite [26,27]. XRPD data were collected on a PANalytical X'Pert Pro (NL) θ/θ diffractometer, equipped with a fast real-time multiple strip (RTMS) detector (PIXcel 1D, PANalytical), using Cu K_α radiation (45 kV and 40 mA) with a virtual step size of 0.02 °2θ and virtual time per step of 200 s over a 20–80 °2θ range. The instrumental broadening was measured using the NIST SRM 660b standard (LaB_6) with data collected under the

same conditions as those used for the TiO_2 specimens. XRPD was also used to determine microstructural features from the specimens. For this purpose, XRPD data were collected in the same instrument with identical set-up as that used for QPA analysis. The angular range 20-145 °2θ was investigated, with virtual time per step of 500 s, to employ data with high signal-to-noise ratio. Microstructural features of the specimens were analysed through the whole powder pattern modelling (WPPM) method [28], as implemented in the PM2K software package [29], using the same modelling strategy as in previous reports by the authors [30,31]. Diffuse reflectance (DR) spectroscopy was used to assess the optical properties of the specimens. DR spectra were recorded on a Shimadzu UV-3100 spectrometer (JP), equipped with an integrating sphere and a white reference material made of Spectralon®, in the UV–Vis spectral range (250–850 nm), with 0.2 nm in resolution. DR spectra were transformed into pseudo-absorption spectra by means of the Kubelka-Munk formalism [32].

The morphology of the aggregates of TiO_2 and $CuO–TiO_2$ was studied using a JEOL JSM-6480LV scanning electron microscope (SEM) with Oxford INCA Energy X-ray Analyser correlated using an acceleration voltage of 20 keV and a spot size of 60 µm. A higher magnification study of the particles was obtained using a Zeiss Orion NanoFab. The images were acquired using He^+ ions with an accelerating voltage of 25kV. High-resolution scanning TEM (HRSTEM) imaging, quantitative spatially-resolved Energy-dispersive X-ray spectroscopy (SR-EDS) analyses and spatially-resolved electron energy-loss spectroscopy (SR-EELS) were performed using a FEI Titan Themis microscope which was operated at 200 kV. The Themis is equipped with a double Cs aberration-corrector, a monochromator, an X-FEG gun, an Ultra High Resolution Energy Filter (Gatan Quantum ERS) which allows working in Dual-EELS mode and a Super X EDS detector, which consists of a 4-windowless detector that can be used independently. To avoid Cu signal arising from the TEM environment during EDS analyses, gold TEM grids were used for the sample preparation and they were mounted on the TEM sample holder by using non Cu-based clips. HRSTEM imaging was performed by using high-angle annular dark-field (HAADF), annular dark-field (ADF) and bright field (BF) detectors. SR-EELS spectra were acquired with an energy dispersion of 0.1 eV.pixel^{-1}, an acquisition time of 0.1 second.pixel^{-1}, and an energy resolution of 0.9 eV. The convergence and collection angles were 21 and 41 mrad, respectively. The EELS spectra were acquired in dual EELS mode allowing for the precise calibration of the spectra and correction of energetic instabilities by recording simultaneously low-loss and core-loss spectra. EELS datasets were processed by using Digital Micrograph and scientific python packages, such as Hyperspy [33], which were used for principal component analysis and chemical mapping.

The specific surface area (SSA) of the prepared samples was determined using the Brunauer–Emmett–Teller (BET) method. Adsorption isotherms were recorded using N_2 as the adsorbate gas, on samples degassed at 120 °C on a Micromeritics Gemini 2380 (US) surface area analyser.

2. 5 Photoelectrochemical glucose sensing tests

Electrochemical measurements were performed in laboratory conditions using commercial screen-printed carbon electrode (SPCE), comprising of a planar substrate equipped with a carbon working electrode (4 mm in diameter, geometric area of 0.1257 cm^2), a silver pseudo-reference electrode and a carbon auxiliary electrode. To modify the bare SPCEs, *** mg of each CuO-TiO_2 nanocomposites were ultrasonically dispersed in distilled water (1 mL). Then, **µl of the homogenous dispersions were directly drop casted onto the surface of the carbon working electrode and left at room temperature to dry until further use. Cyclic voltammetry (CV) and amperometry (*I*-t) techniques were applied at DropSens μStat 400 potentiostat empowered by Dropview 8400 software for data acquisition. All experiments were performed at room temperature unless otherwise stated, under dark, ambient light and halogen lamp (50 W).

3 RESULTS AND DISCUSSION

3.1 Morphological characterisation

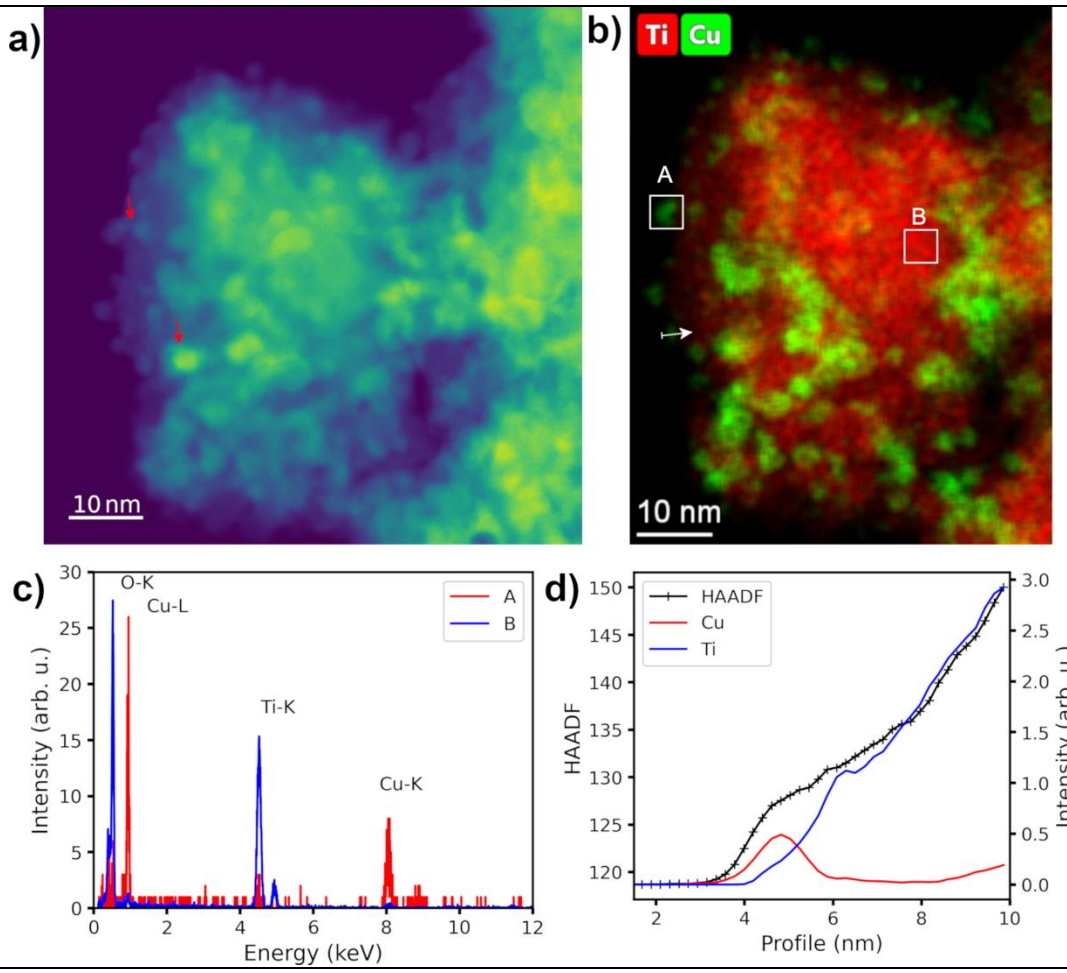

Figure 1. STEM analyses of the sample **Ti1.00:Cu0.25** a) STEM-HAADF image; b) EDS chemical maps; c) corresponding EDS spectra extracted from the areas highlighted by the white squares on the chemical map; d) HAADF, Cu and Ti intensity profiles extracted from the area highlighted by the white arrow in the chemical map.

Figures S3 shows an HR-STEM BF micrograph acquired on the sample **Ti1.00:Cu0.25**. The NPs have a size < 5 nm, with a high crystalline quality. Figure 1a displays a STEM HAADF micrograph acquired on the same sample. A local increase in intensity can be highlighted in the micrograph (red arrows in Figure 1a), which points out a local increase in the mass density and/or a local increase in thickness, thus suggesting the presence of Cu-based NPs. However, direct interpretation of intensity variations in this image is not straightforward due to thickness variations of agglomerated grains. To get more insight on the microstructure of CuO–TiO_2 samples, SR-EDS analysis was performed in the same area (Figure 1b). The presence of Cu-rich and Ti-rich separated areas are clearly visible in the EDS chemical maps, and in the corresponding EDS spectra (Figure 1c). In particular, the presence of Cu-based clusters at the surface of TiO_2 NPs can be clearly highlighted in the intensity profile (Figure 1d). These clusters have a typical size of about one nanometre, and can be seen as larger agglomerates in

thicker parts of the sample. To confirm these results, SR-EELS analysis were also performed on the same area. Figure S4a shows the Cu-$L_{2,3}$ edge integrated intensity EELS map. There is an excellent agreement between the EELS and EDS results. Figure S4b shows the Cu-$L_{2,3}$ EELS edge fine structures acquired on a Cu-based nanoparticle with a size of about 6 nm. Cu-$L_{2,3}$ fine structures can be used to discriminate the chemical local environment of the copper, and to distinguish between metallic copper, CuO and Cu_2O [34]. The EELS spectrum displayed in Figure S4b shows a fine structure retaining an intermediate behaviour between metallic copper and a coper oxide. To check the presence of spatial inhomogeneity in the copper local chemical environment, the experiment was repeated at higher magnification, and with a better spatial resolution. Figure 2 shows the SR-EELS analysis performed on an individual Cu-based NP with a size of about 4.7 nm. The Cu-$L_{2,3}$ fine structures of the core part of the particle presents a plateau, typical of metallic copper. On the other hand, the Cu-$L_{2,3}$ fine structures of the spectrum acquired at the surface of that NP clearly shows a peak at around 930 eV, which is common of a copper oxide. Due to the signal-to-noise ratio, distinguishing between CuO and Cu_2O is not straightforward. However, there is shift of about 2.5 eV between the peak acquired at the surface of the NP, and the left side of the plateau, which indicates the presence of CuO at the surface of the NP. All these results show the strong intertwining between the TiO_2 NPs and the Cu-based NPs. The Cu-based NPs have a size < 5 nm, and present a metallic core with a CuO rich surface. Figure S5 shows the STEM analysis performed on the sample **Ti1.00:Cu0.50**. In this case, in addition of the small Cu-based NPs, bigger NPs with a size of about 10 nm were also observed, suggesting a non-ideal distribution of the NPs.

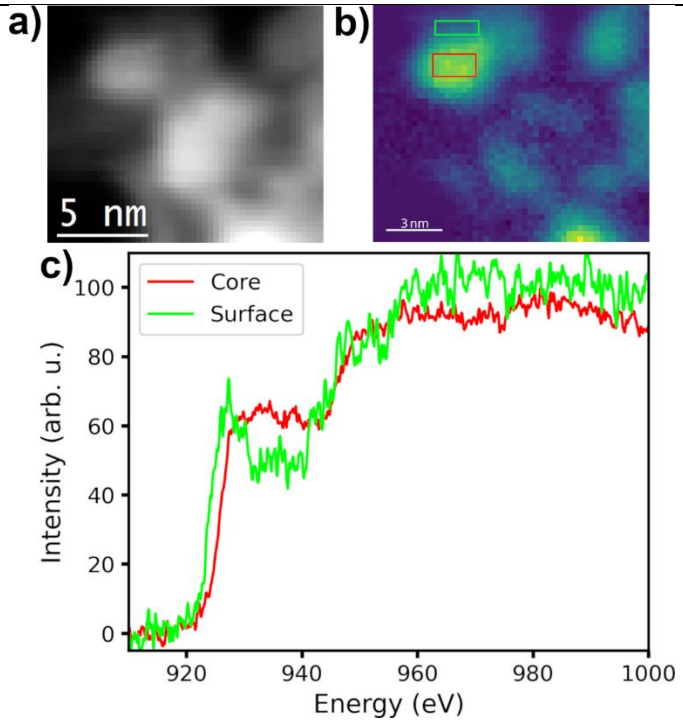

Figure 2. SR-EELS analyses of the sample **Ti1.00:Cu0.25** a) STEM-ADF micrograph acquired simultaneously as the EELS dataset; b) Cu-$L_{2,3}$ edge integrated intensity map; c) EELS spectra acquired at the core and surface of a Cu-based NP, in the areas highlighted by red and green rectangles, respectively, on the corresponding EELS chemical map.

3.2 Microstructural characterization

XRPD patterns of the CuO–TiO_2 samples are reported in Figure 3. A graphical output of a Rietveld refinement is shown in Figure S6. Information about the crystalline component in the set of prepared specimens, as obtained using Rietveld QPA refinement of XRPD data, is listed in Table 1.

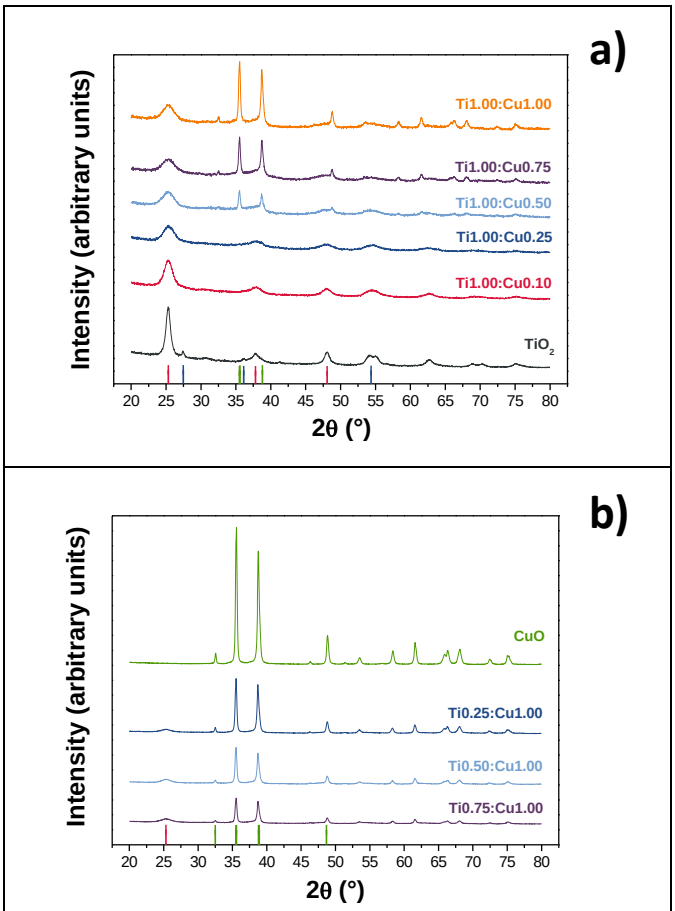

Figure 3. XRPD patterns of the CuO–TiO_2 samples. a) **TiO_2** and CuO–TiO_2 specimens having TiO_2 molar amounts ≥ than CuO. The vertical bars represent the three most intense reflections of: anatase (red), rutile (blue), tenorite (green). b) XRPD patterns of **CuO** (tenorite), and CuO–TiO_2 specimens having TiO_2 molar amounts < than CuO. The vertical bars represent the most intense reflection of anatase (red), and the five most intense reflections of tenorite (green).

Table 1. Rietveld agreement factors and phase composition (QPA) of the prepared specimens.

Sample	No. of variables	Agreement factors				Phase composition (wt%)			
		$R(F^2)$ (%)	R_{wp} (%)	χ^2		anatase	rutile	brookite	tenorite
TiO_2	19	3.91	3.79	1.66		83.3±0.1	6.9±0.3	9.8±0.4	–
Ti1.00:Cu0.10	17	4.68	3.14	1.42		90.5±0.1	3.0±0.5	6.4±0.8	–
Ti1.00:Cu0.25	20	3.21	3.29	1.44		99.6±0.1	–	–	0.4±0.2
Ti1.00:Cu0.50	20	7.43	3.26	1.75		85.8±0.2	–	–	14.2±0.2
Ti1.00:Cu0.75	21	5.59	3.49	1.89		77.1±0.4	–	–	22.9±0.2
Ti1.00:Cu1.00	21	6.45	4.45	2.13		64.1±0.6	–	–	35.9±0.2
Ti0.75:Cu1.00	18	8.54	2.67	3.61		39.0±0.5	–	–	61.0±0.1
Ti0.50:Cu1.00	18	9.38	2.79	4.55		29.5±0.5	–	–	70.5±0.1
Ti0.25:Cu1.00	18	8.45	2.97	6.07		19.0±0.6	–	–	81.0±0.1
CuO	17	4.75	3.62	13.85		–	–	–	100

Note: there were 2285 observations for every refinement; the number of anatase, rutile, brookite and tenorite reflections was 32, 31, 154 and 48, respectively.

Titania specimen is composed of anatase (83.3 wt%), rutile (6.9 wt%) and brookite (9.8 wt%) TiO_2 polymorphs. Presence of brookite is not unexpected, as it is a frequent "by-product" when the synthesis is performed in acidic media [35]. Anatase is the thermodynamically stable TiO_2 polymorph on the nanoscale [36]. However, both anatase and brookite are TiO_2 metastable polymorphs, and transform irreversibly themselves to rutile when they are subjected to thermal treatment.

Addition of copper retarded the anatase-to-rutile phase transition (ART). When the TiO_2:CuO molar ratio was 1.00:0.10 (**Ti1.00:Cu0.10**), we had: 90.5 wt% anatase, 3.0 wt% rutile, the remaining wt% being brookite. At this modification level, CuO was not detected by XRPD. Specimen **Ti1.00:Cu0.25** was only composed by anatase (99.6 wt%) and traces of tenorite (CuO, 0.4 wt%). Increasing the amount of copper in the system led to an increased amount of tenorite, this latter accounting for 35.9 wt% (together with 64.1 wt% anatase) in the specimen in which the TiO_2:CuO molar ratio was 1.00:1.00 (**Ti1.00:Cu1.00**). That trend continued in specimens having TiO_2 molar amounts lower than those of CuO: 39.0 wt% anatase together with 61.0 wt% tenorite in **Ti0.75:Cu1.00**. To reach 81.0 wt% tenorite and 19.0 wt% anatase in **Ti0.25:Cu1.00**. This means that introducing copper in the TiO_2 system led to a grain-boundary pinning (*i.e.* Zener pinning) [37], which eventually culminates in totally delaying the ART – the onset of it being specimen **Ti1.00:Cu0.25**.

Microstructural information as obtained by means of the WPPM formalism are reported in Tables 2 and 3 and Figure 4a-d; an example of WPPM graphical output is shown in Figure S7. From the virtually nil differences in unit cell volumes (*cf* Table 2), we can discard any Cu^{2+} entrance in the TiO_2 structure and *vice-versa* (*i.e.* Ti^{4+} entrance in the tenorite structure) [30,37]. However, the presence

of copper in the TiO_2-CuO system led to a considerable decrease in the average diameter of anatase crystalline domains. Indeed, looking at the values tabulated in Table 3, anatase in the unmodified specimen had 8.0 nm in average diameter. This decreased to 4.4 nm in **Ti1.00:Cu0.10**, up to 3.3 nm in **Ti1.00:Cu1.00**. On the contrary, increasing the relative CuO amount led to a faster nucleation and growth of CuO crystals. The average diameter of CuO was 5.3 nm in **Ti1.00:Cu0.50**, going to 36.9nm in **Ti0.25:Cu1.00**, see Table 3. As for CuO crystals, their average diameter is 40.1 nm in **CuO** specimen.

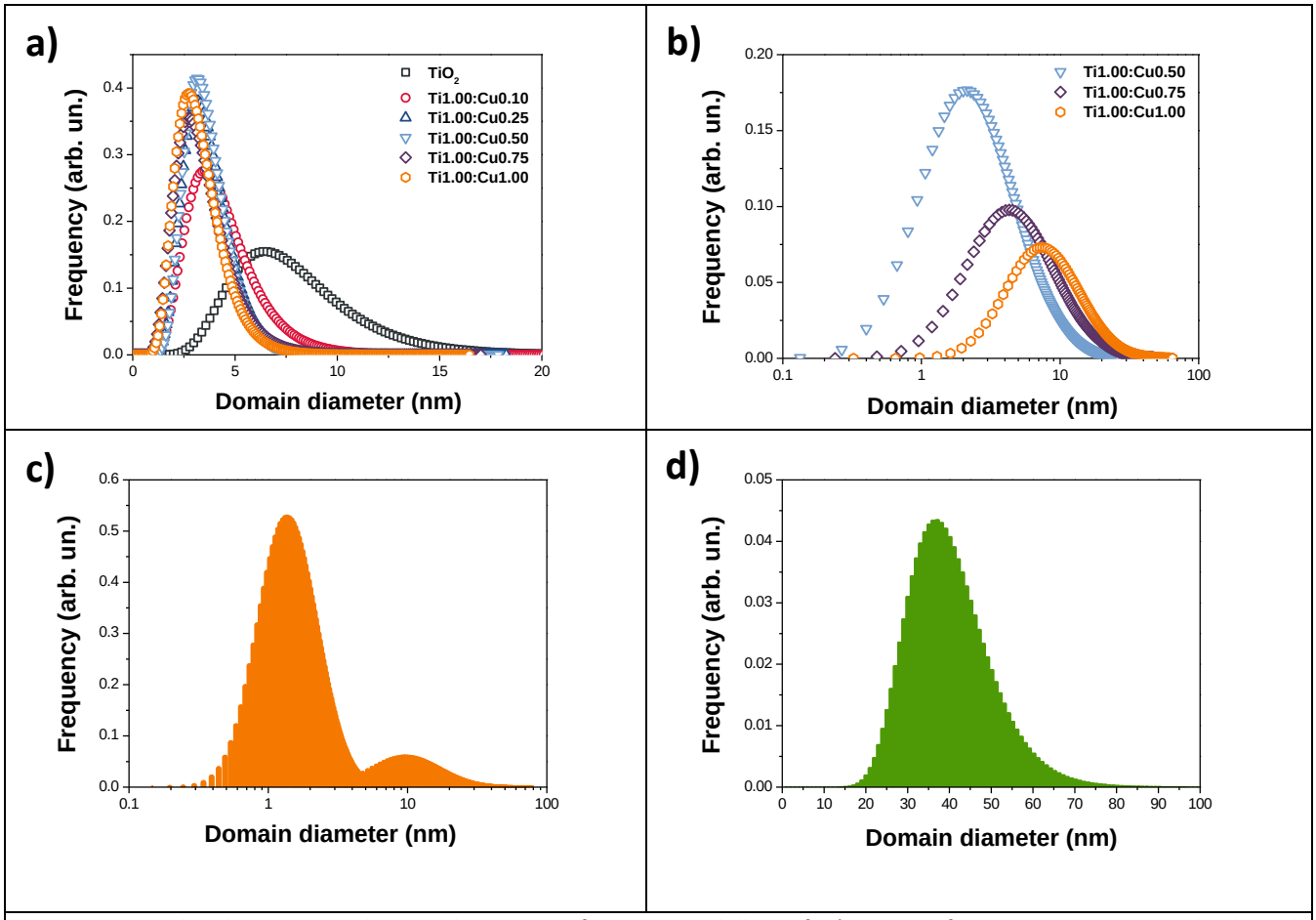

Figure 4. Size distributions, as obtained by means of WPPM modelling of: a) anatase fraction in the **TiO_2** and selected TiO_2–CuO specimens. b) CuO fraction in TiO_2–CuO specimens, according to a unimodal model. c) CuO fraction in specimen **Ti1.00:Cu1.00**, according to a bimodal model. Size reported in log-scale in b) and c). d) tenorite in specimen **CuO**.

Table 2 – WPPM agreement factors and unit cell parameters for anatase (TiO_2) and tenorite (CuO) mineralogical phases in synthesised samples.

Sample	Agreement factors			Unit cell parameters							
	R_{wp} (%)	R_{exp} (%)	χ^2	Anatase			Tenorite				
				a=b (nm)	c (nm)	V (nm³)	a (nm)	b (nm)	c (nm)	β (°)	V (nm³)
TiO_2	3.01	2.63	1.14	0.3789(1)	0.9512(3)	0.137(1)					–
Ti1.00:Cu0.10	2.71	2.35	1.16	0.3796(3)	0.9499(12)	0.137(2)					–
Ti1.00:Cu0.25	2.18	2.04	1.07	0.3789(7)	0.9508(18)	0.137(3)					–
Ti1.00:Cu0.50	2.25	1.78	1.27	0.3788(3)	0.9557(17)	0.137(2)	0.4691(2)	0.3435(2)	0.5136(2)	99.5(1)	0.082(1)
Ti1.00:Cu0.75	2.58	2.11	1.22	0.3787(2)	0.9447(29)	0.136(1)	0.4692(1)	0.3429(1)	0.5129(1)	99.4(1)	0.081(1)
Ti1.00:Cu1.00	2.53	1.98	1.27	0.3785(3)	0.9551(17)	0.137(2)	0.4691(1)	0.3436(1)	0.5133(1)	99.5(1)	0.082(1)
Ti0.75:Cu1.00	1.70	1.23	1.38	0.3779(2)	0.9521(11)	0.136(1)	0.4688(1)	0.3431(1)	0.5130(1)	99.5(1)	0.081(1)
Ti0.50:Cu1.00	1.78	1.15	1.54	0.3780(2)	0.9557(7)	0.137(1)	0.4688(1)	0.3432(1)	0.5131(1)	99.5(1)	0.081(1)
Ti0.25:Cu1.00	1.92	1.06	1.80	0.3776(2)	0.9553(4)	0.136(1)	0.4689(1)	0.3432(1)	0.5133(1)	99.4(1)	0.081(1)
CuO	3.25	0.88	3.70			–	0.4691(1)	0.3434(1)	0.5132(1)	99.5(1)	0.082(1)

Table 3 – Mean crystalline domain size of anatase (ant) and tenorite (tnr) – defined as the mean of the lognormal size distributions; maximum values (mode), median, skewness of the lognormal size distributions, and polydispersity index (PDI, $Đ$), as derived from the WPPM method. Specific surface area values of the specimens are reported in the last column.

Sample	Mean crystalline domain diameter		Mode of the size distribution		Median of the size distribution		Skewness of the size distribution		$Đ$		SSA_{BET} (m².g⁻¹)
	$\langle D_{ant} \rangle$ (nm)	$\langle D_{tnr} \rangle$ (nm)	Ant (nm)	Tnr (nm)	Ant (nm)	Tnr (nm)	Ant (nm)	Tnr (nm)	Ant (nm)	Tnr (nm)	
TiO_2	8.0±0.6	–	6.5±0.5	–	7.4±0.5	–	1.2±0.1	–	0.15±0.02	–	64.6±0.9
Ti1.00:Cu0.10	4.4±0.2	–	3.5±0.1	–	4.1±0.2	–	1.2±0.1	–	0.16±0.04	–	88.2±1.0
Ti1.00:Cu0.25	3.7±0.3	–	3.2±0.2	–	3.5±0.3	–	1.0±0.1	–	0.10±0.06	–	103.2±1.2
Ti1.00:Cu0.50	3.6±0.3	5.3±0.3	3.2±0.3	2.1±0.1	3.4±0.3	3.9±0.2	0.9±0.1	3.6±0.1	0.09±0.05	0.86±0.08	96.9±1.2
Ti1.00:Cu0.75	3.4±0.1	9.3±0.5	2.8±0.1	4.1±0.2	3.2±0.2	7.1±0.4	1.2±0.1	3.1±0.4	0.15±0.06	0.72±0.10	94.5±1.1
Ti1.00:Cu1.00	3.3±0.5	13.0±0.6	2.7±0.8	7.4±0.3	3.1±0.4	10.8±0.5	1.1±0.2	2.3±0.2	0.13±0.05	0.45±0.06	79.9±0.8
Ti0.75:Cu1.00	3.5±0.5	23.5±0.6	2.7±0.5	16.9±0.5	3.2±0.5	21.0±0.6	1.4±0.1	1.6±0.1	0.18±0.01	0.24±0.04	55.9±0.6
Ti0.50:Cu1.00	3.6±0.1	35.6±4.5	2.7±0.1	32.0±4.1	3.3±0.1	34.4±4.4	1.5±0.1	0.8±0.1	0.22±0.01	0.07±0.04	44.6±0.4
Ti0.25:Cu1.00	3.5±0.1	36.9±4.3	2.5±0.1	32.3±4.0	3.1±0.1	35.3±4.2	1.6±0.1	0.9±0.1	0.24±0.01	0.09±0.01	27.5±0.3
CuO	–	40.1±2.1	–	36.7±1.9	–	39.0±2.0	–	0.8±0.1	–	0.06±0.03	1.4±0.2

However, CuO nanocrystals in the CuO–TiO_2 specimens are likely polydisperse, as suggested by the STEM analyses. Indeed, looking at the output of the WPPM modelling (specimen **Ti1.00:Cu1.00**), adopting a monodisperse model, does not lead to a perfect fit, as some features are still present in the difference curve. This might be due to a non-ideal distribution of CuO coherently diffracting domains. Thus, we adopted a bimodal model for the size distribution of CuO in the TiO_2–CuO system. This led to a better fit, as shown in Figures S7,S8, Table S1, and Figure 4c. For instance, the size distribution of CuO in **Ti1.00:Cu1.00** adopting a bimodal size distribution model showed small CuO NPs (average diameter ~2.0 nm) together with bigger CuO NPs (having ~16.0 nm in average diameter). Furthermore, as can be noted, the absence of TiO_2 in the TiO_2-CuO system, led to a faster nucleation and growth of CuO crystals. As shown in Figure 4d, the average diameter of the CuO NPs is ~40 nm.

3.3 Optical properties

DRS spectra of prepared specimens are reported in Figure S9. Unmodified TiO_2 shows a single absorption feature at < 400 nm, ascribed to the band gap transition in titania [32]. Adding CuO to TiO_2 led to modification in the optical properties of the specimens. The strong absorption band seen at lower energies and centred at ~850 nm in **Ti1.00:Cu0.10** and **Ti1.00:Cu0.25**, belongs to *d*–*d* electronic transition in Cu^{2+} [38]. This band shifts itself to higher energies as the CuO molar amount increases, up to reach a maximum at around 750 nm, and becoming the only band detectable in tenorite (specimen **CuO**). A further absorption feature, placed at around 450 nm, is detectable in the CuO–TiO_2 specimens. This belongs to interfacial charge transfer (IFCT) processes – an electron transferring from the valence band of TiO_2 to the CuO clusters that are grafted around titania [39].

3.4 Electrochemical tests

The electrochemical behaviour of modified CuO/TiO_2/SPCE electrodes in the presence of glucose was investigated by performing CV in 0.1 M KOH solution in the range of potential 0–1 V, at a scan rate of 50 $mV.s^{-1}$. Examples of tests performed with different CuO–TiO_2 specimens are shown in Figure 6. Tests were carried out in ambient conditions of temperature and laboratory illumination. Preliminary, no peak and/or significant current variation was observed on TiO_2/SPCE electrode in the

presence of glucose concentrations up to 10 mM. Data reported shows instead clearly that the modified CuO/TiO_2/SPCE electrodes exhibit significant variation in the oxidation of glucose. A broad anodic peak, due to the irreversible glucose oxidation, is indeed observed at CuO/TiO_2/SPCE electrodes. The oxidation current starts to increase at approximately 0.35–0.45 V, and shows an anodic peak at 0.70–0.85 V.

Data also clearly show that the current variation linked to glucose oxidation is strictly dependent on CuO loading. This confirms that this latter species acts as the precursor of active sites in the electro-oxidation of glucose in alkaline environment, in agreement with previous reports [21]. In detail, an increase in the oxidation peak current with CuO loading is observed. The highest response was noted for the CuO/SPCE electrode, which is obviously related to higher amount of CuO active sites available for the glucose oxidation. This finding is well confirmed by the shift of the oxidation peak *versus* the lower potential, with increasing the CuO loading, from 0.82 V to 0.71 V.

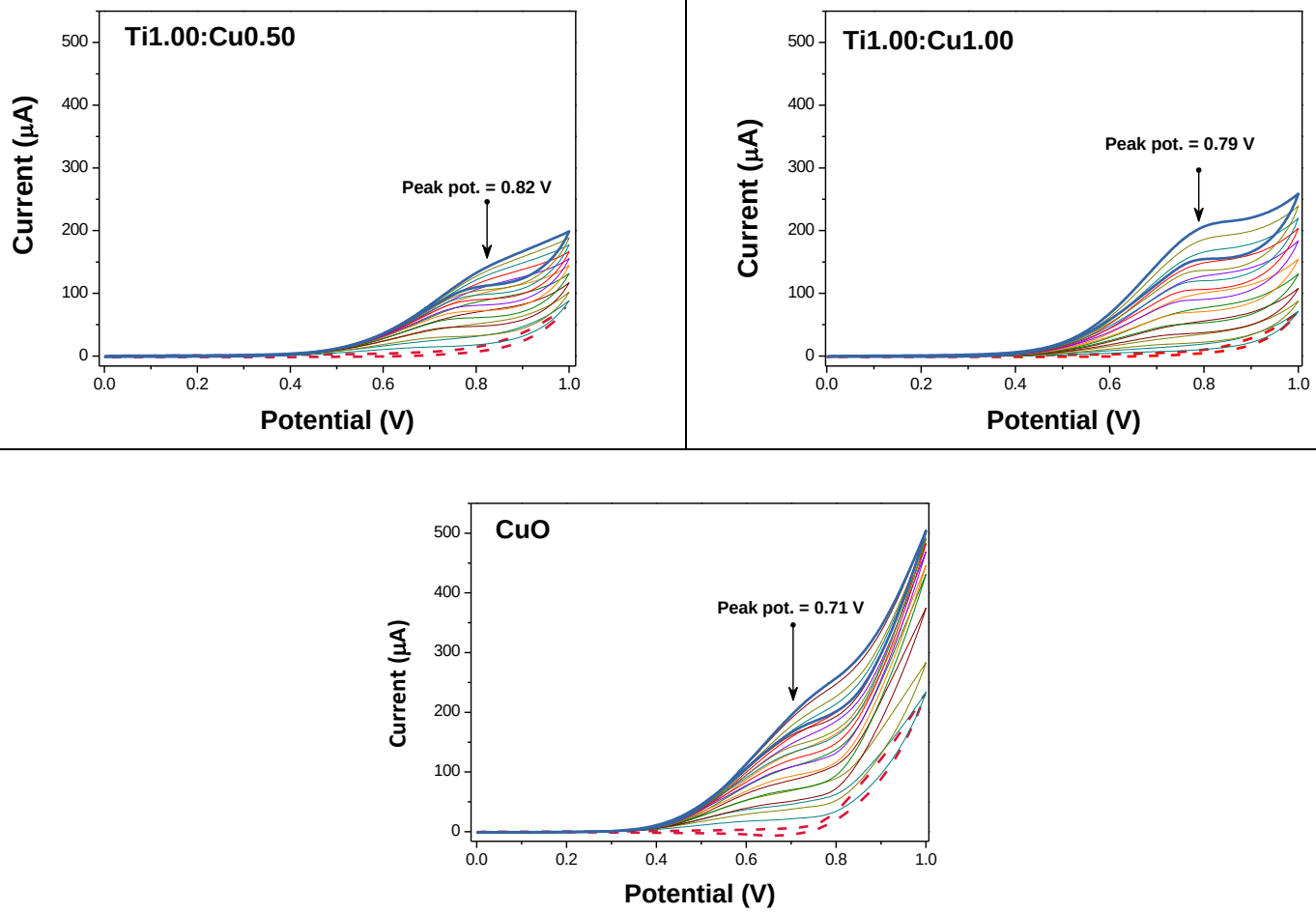

Figure 6. Electrochemical behaviour of modified CuO/TiO_2/SPCE electrodes in the presence of glucose between 0 and 10 mM. Potential range = 0-1 V; electrolyte = 0.1 M KOH solution; scan rate = 50 $mV.s^{-1}$.

Calibration curves obtained with the different CuO–TiO_2 specimens, in the glucose concentration range between 0 and 10 mM, under ambient condition, are reported in Figure 7.

CuO–TiO_2 heterojunctions have been widely used as composite photocatalysts [13]. Under illumination, the CuO–TiO_2 *p–n* heterojunction results in the injection of electrons in the TiO_2 conduction band and accumulation of holes in the narrower CuO band gap semiconductor valence band (creating strong oxidant sites). This process is expected to provide a better charge separation, which could also increase the charge transport efficiency, leading to an efficient photo-electrocatalysts.

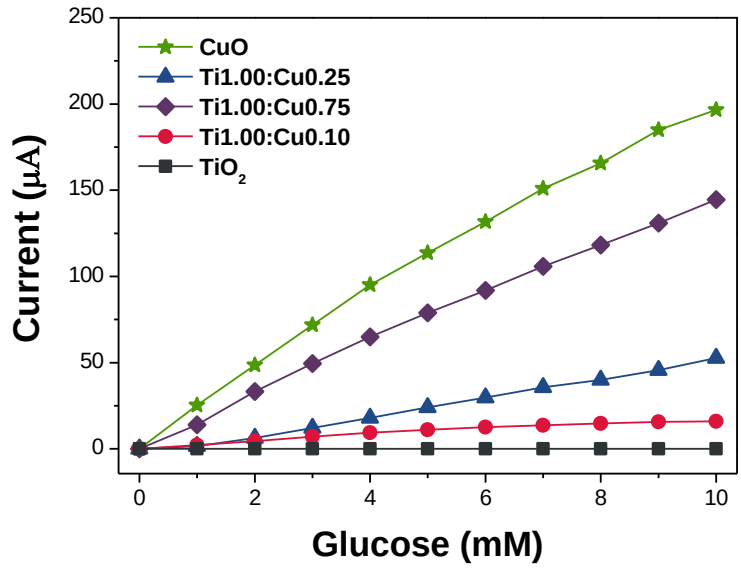

Figure 7. Calibration curves for various CuO–TiO_2/SPCE electrodes as a function of glucose concentration.

Out on this basis, we have tried to verify if direct irradiation of CuO/TiO_2/SPCE electrodes could be advantageous to further improve glucose oxidation. Then, these electrodes have been tested under the irradiation of a halogen lamp (50 W). Figure 8a shows the current value in **Ti1.00:Cu0.10** sensor as function of glucose concentration, for different light conditions, compared to standard ambient condition. Results obtained in dark have been also reported for comparison.

The slight increase of current observed with **Ti1.00:Cu0.10** under ambient illumination, compared to dark condition, suggests that visible light has an effect on the sensitivity towards glucose. It can be also clearly observed that the tested CuO–TiO_2 electrode, directly irradiated with halogen light,

exhibits a more pronounced effect, indicating that the use of halogen light enhance remarkably the oxidation of glucose. Examining the calibration curves obtained on some CuO/TiO_2/SPCE electrodes (Figure 8b), it appears clear as the effect of illumination is strictly linked to CuO/TiO_2 composition. First, it is noteworthy that illumination with halogen light is irrelevant in order to improve glucose current on both TiO_2/SPCE and CuO/SPCE electrodes, thus meaning that CuO–TiO_2 *p*–*n* heterojunction is essential in this context. Indeed, with CuO/TiO_2/SPCE electrodes in the presence of CuO, the current increases remarkably under halogen lamp illumination. The relative improvement is then related to CuO–TiO_2 composition.

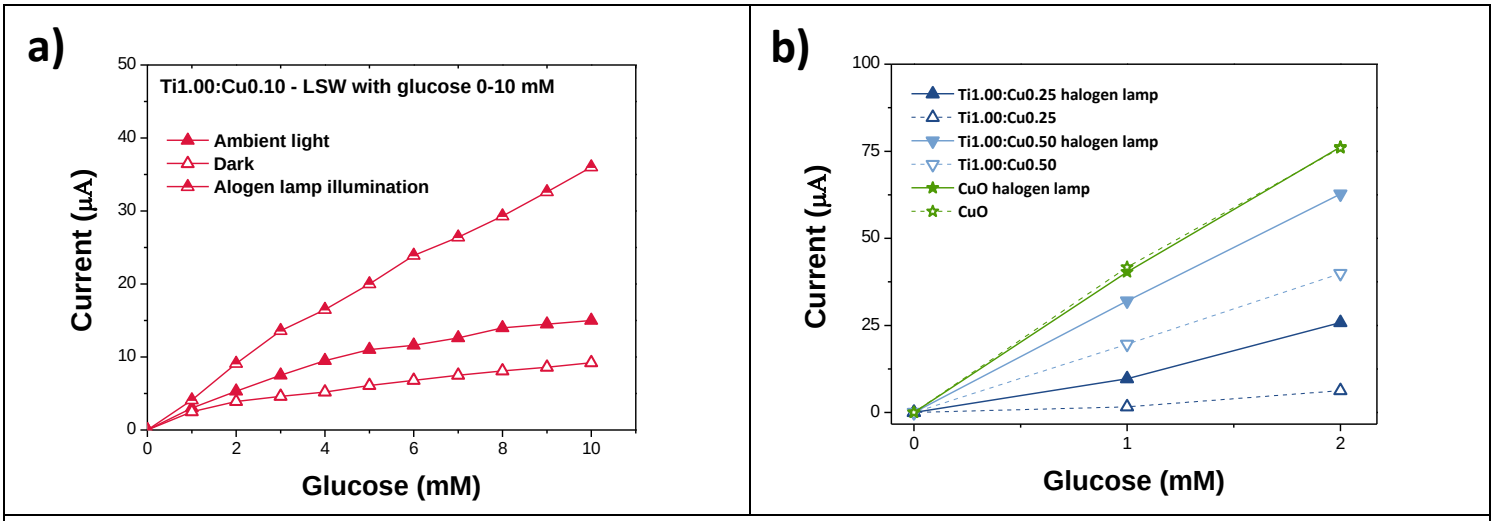

Figure 8. a) Calibration curves for **Ti1.00:Cu0.10** SPCE electrode, operating in different conditions, as a function of glucose concentration. b) Calibration curves for different TiO_2 loadings, under illumination, and with no light. No difference in glucose sensitivity is noticeable in the specimen made of only CuO.

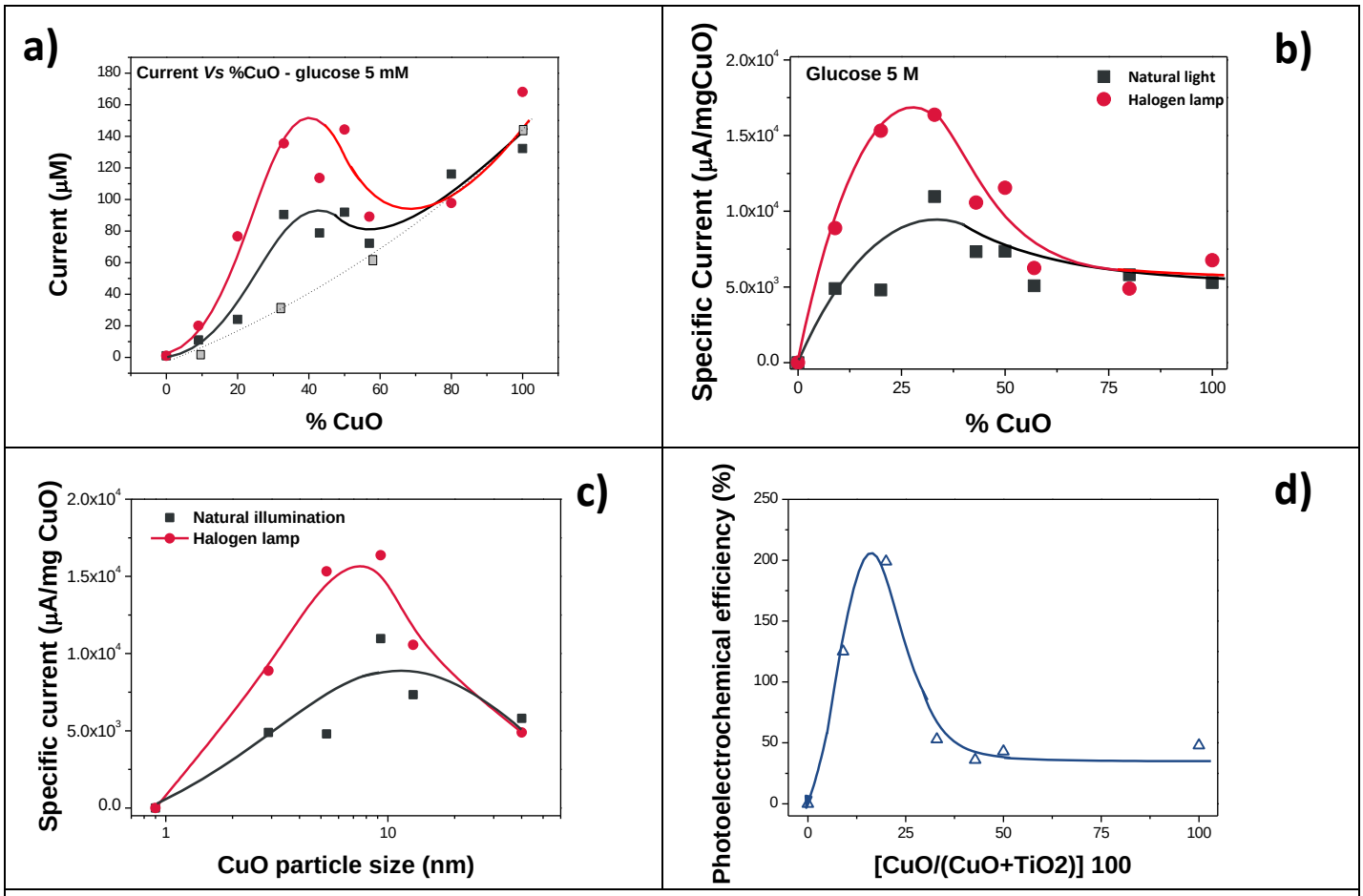

Figure 9. a) Comparison of the electrochemical responses to glucose under different illumination conditions (dark, ambient and halogen light illumination) as a function of CuO loading. b) Comparison of the specific electrochemical responses to glucose under ambient and halogen light illumination as a function of CuO loading. c) Comparison of the specific electrochemical responses to glucose under ambient and halogen light as a function of CuO particle size. d) Photoelectrochemical efficiency for the investigated glucose sensors as a function of CuO loading.

To better understand this aspect, we collected all the data related to glucose current derived by CV performed in the conditions above described (see Figure 9a).

If we report the obtained response normalised to the quantity of the CuO active sites, the CuO–TiO_2 specimens display better performances compared with pure CuO specimen (Figure 9b). Data also revealed that there is a dependence of the response with the CuO particle size (Figure 9c). The curve obtained indicates that the best PEC response is linked to the presence of very small CuO particles. This is particularly evident in Figure 9d, where the photochemical efficiency, *i.e.* the ratio between the current response in light and under ambient illumination, is plotted as a function of the CuO molar ratio. A strong increase in the photochemical efficiency appeared at around 20 mol% CuO (**Ti1.00:Cu0.20**), which is attributed to the optimal combination of CuO amount and small particle size.

1.3.4. Quantitative determination of glucose

Quantitative analysis of glucose is essential in clinical, pharmaceutical and industrial sectors [40]. To evaluate the ability of the sensor developed for the quantitative detection of glucose, the linear sweep voltammetry (LSV) technique was used here. Potential sweeps were done at 50 $mV.s^{-1}$, beginning at 0.3 V, and sweeping up to 1.0 V. As an example, the quantitative determination of glucose on the **Cu-TiO_2 electrode, registered adding successively different glucose amounts to the 0.1 M KOH electrolyte solution, is shown in Figure 10.

It is noteworthy that, increasing the concentration of glucose, the oxidation potential shifts towards more positive values, due to kinetic limitations at the electrode surface. It can be supposed that the detection mechanism involved during the LSV process in alkaline medium, follows first the generation of the active site layer, *i.e.* CuOOH, on the surface of **Cu-TiO_2 electrode. Then, the oxidation of glucose to gluconolactone catalysed by the CuO/CuOOH redox couple leads to an increase of anodic current:

Cu(II)O → Cu(III)OOH

Cu(III)OOH + glucose → CuO(II) + gluconolactone

Cu(III)OOH specie acts as an electron transfer mediator for the oxidation of glucose [41], revealing the strong electrocatalytic activity of Cu species towards glucose oxidation.

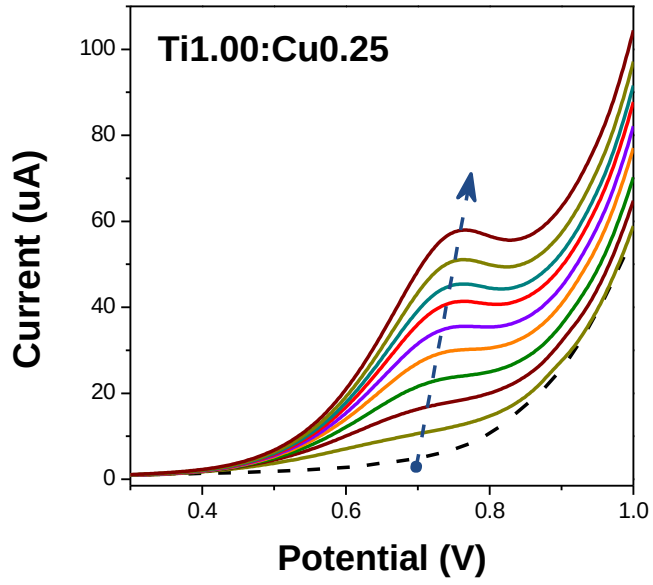

Figure 10. LSV registered adding successively different glucose amounts to the 0.1 M KOH electrolyte solution on the **Cu-TiO2 electrode.

The calibration curve for some of the electrodes is reported in Figure 11. This shows almost a linear relationship (R^2= ****) between current intensity and glucose concentration up to 10 mM – glucose having a regression equation: I (μA) = 12.78 × $C_{glucose}$ (mM) + 6.61. The limit of detection (LOD) estimated from the calibration curve for the sensor was *** μM (at S/N = 3), and the calculated sensitivity was *** μA.mM^{-1}.cm^{-2}.

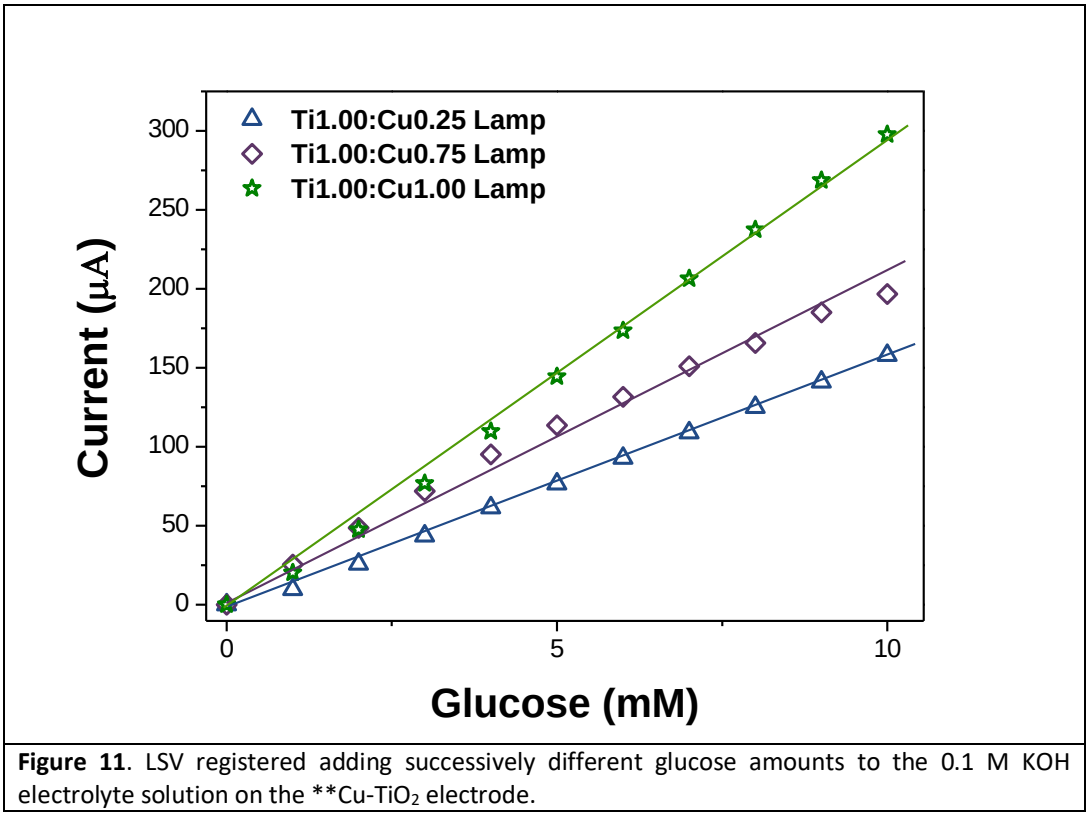

Figure 11. LSV registered adding successively different glucose amounts to the 0.1 M KOH electrolyte solution on the **Cu-TiO_2 electrode.

In the literature there are many papers dealing with non-enzymatic glucose sensors based on several copper nanostructures [***]. The performances of the sensor fabricated in this work were thus compared with other non-enzymatic glucose sensors, revealing that the former are consistent with, or even better than those reported in recent literature (see Table 1).

Table 1 – Analytical parameters of glucose non-enzymatic electrochemical biosensors using various copper nanostructures.

Electrode	Modifier	Detection potential (mV)	Sensitivity $\mu A/mM.cm^{-2}$	Detection limit (μM)	Refs
GCE	Cu(NP)-graphene	500	157.2	0.5	[42]
GCE	Cu/PEI/MWCNTs	350	714.4	0.5	[43]
GCE	CuO nanocubes–graphene	590	1360	0.7	[44]
Cu foil	$Cu(OH)_2$ nanotubes	400	418	0.5	[41]
GTE	Cu nanowires	550	1100	1.6	[45]
GCE	Cu_2O/NiO_x/graphene oxide	600	285	0.4	[46]
GCE	CuO/mesoporous carbon	450	1154.1	0.1	[47]
TiO_2	Cu/Ni (NP)	600	1590.9	5	[48]
GCE	CuO/graphene	600	1065	1	[49]
SPCE	**CuO–TiO_2**	**700**	***	**	**This work**

GCE = glassy carbon electrode; GTE = graphene transparent electrode; MWCNTs = multi-walled carbon nanotubes; NP = nanoparticles; PEI = polyethylenimine.

Results suggest that TiO_2 provides a large surface area for CuO, which in turn enhances electrochemical activity for glucose detection. The PEC sensing electrode exhibited remarkable high performance in terms of sensitivity, wide response range, response time, selectivity, reproducibility, repeatability, and stability.

4 CONCLUSIONS

To summarise, CuO nanoparticles decorating TiO_2 particles are effective in promoting glucose oxidation reaction in alkaline media. Apart this electrocatalytic effect, we also demonstrated that they are very effective in operating under (halogen lamp) illumination. The improved performances of CuO/TiO_2/SPCE electrodes may be mainly associated to the *p*–*n* junction between CuO and TiO_2 nanoparticles, which enhances the photocurrent density by promoting charge separation.

The performance of CuO/TiO_2/SPCE electrodes for quantitative determination of glucose was also reported using LSV, determining the sensitivity, linear concentration range and LOD. The high sensitivity obtained shows that the CuO/TiO_2/SPCE is very much suitable for use as a transducer layer for non-invasive glucose monitoring.

5 Acknowledgments

This work was partly developed within the scope of the project CICECO–Aveiro Institute of Materials, UIDB/50011/2020 & UIDP/50011/2020, financed by national funds through the FCT/MEC and when appropriate co-financed by FEDER under the PT2020 Partnership Agreement. David Maria Tobaldi, although "*not so young*" and/or "*not having given a sufficient level of relevance and impact on the scientific community considering his age*", is very much grateful to FCT and to Portuguese national funds (OE), through FCT, I.P., in the scope of the framework contract foreseen in the numbers 4, 5 and 6 of the article 23, of the Decree-Law 57/2016, of August 29, changed by Law 57/2017, of July 19. This project has also received partial funding from the European Union's Horizon 2020 research and innovation programme under grant agreement No 823717 – ESTEEM3. We are obliged to Miss Dafne Maria Glaglanon for proof editing the English of the manuscript.

6 References

[1] B.L. Allen, P.D. Kichambare, A. Star, Carbon Nanotube Field-Effect-Transistor-Based Biosensors, Advanced Materials. 19 (2007) 1439–1451. https://doi.org/10.1002/adma.200602043.

[2] A. Chen, S. Chatterjee, Nanomaterials based electrochemical sensors for biomedical applications, Chem. Soc. Rev. 42 (2013) 5425. https://doi.org/10.1039/c3cs35518g.

[3] S. Park, H. Boo, T.D. Chung, Electrochemical non-enzymatic glucose sensors, Analytica Chimica Acta. 556 (2006) 46–57. https://doi.org/10.1016/j.aca.2005.05.080.

[4] D.-W. Hwang, S. Lee, M. Seo, T.D. Chung, Recent advances in electrochemical non-enzymatic glucose sensors – A review, Analytica Chimica Acta. 1033 (2018) 1–34. https://doi.org/10.1016/j.aca.2018.05.051.

[5] H. Zhu, L. Li, W. Zhou, Z. Shao, X. Chen, Advances in non-enzymatic glucose sensors based on metal oxides, Journal of Materials Chemistry B. 4 (2016) 7333–7349. https://doi.org/10.1039/C6TB02037B.

[6] K. Tian, M. Prestgard, A. Tiwari, A review of recent advances in nonenzymatic glucose sensors, Materials Science and Engineering: C. 41 (2014) 100–118. https://doi.org/10.1016/j.msec.2014.04.013.

[7] S.G. Leonardi, S. Marini, C. Espro, A. Bonavita, S. Galvagno, G. Neri, In-situ grown flower-like nanostructured CuO on screen printed carbon electrodes for non-enzymatic amperometric sensing of glucose, Microchim Acta. 184 (2017) 2375–2385. https://doi.org/10.1007/s00604-017-2232-1.

[8] S. Marini, N. Ben Mansour, M. Hjiri, R. Dhahri, L. El Mir, C. Espro, A. Bonavita, S. Galvagno, G. Neri, S.G. Leonardi, Non-enzymatic Glucose Sensor Based on Nickel/Carbon Composite, Electroanalysis. 30 (2018) 727–733. https://doi.org/10.1002/elan.201700687.

[9] A. Heller, B. Feldman, Electrochemical Glucose Sensors and Their Applications in Diabetes Management, Chem. Rev. 108 (2008) 2482–2505. https://doi.org/10.1021/cr068069y.

[10] WHO, Diabetes Fact Sheet, (n.d.). https://www.who.int/news-room/fact-sheets/detail/diabetes.

[11] H. Chen, G. Fan, J. Zhao, M. Qiu, P. Sun, Y. Fu, D. Han, G. Cui, A portable micro glucose sensor based on copper-based nanocomposite structure, New J. Chem. 43 (2019) 7806–7813. https://doi.org/10.1039/C9NJ00888H.
[12] A. Fujishima, T.N. Rao, D.A. Tryk, Titanium dioxide photocatalysis, Journal of Photochemistry and Photobiology C: Photochemistry Reviews. 1 (2000) 1–21. https://doi.org/10.1016/S1389-5567(00)00002-2.
[13] J.F. de Brito, F. Tavella, C. Genovese, C. Ampelli, M.V.B. Zanoni, G. Centi, S. Perathoner, Role of CuO in the modification of the photocatalytic water splitting behavior of TiO2 nanotube thin films, Applied Catalysis B: Environmental. 224 (2018) 136–145. https://doi.org/10.1016/j.apcatb.2017.09.071.
[14] A. Devadoss, P. Sudhagar, C. Terashima, K. Nakata, A. Fujishima, Photoelectrochemical biosensors: New insights into promising photoelectrodes and signal amplification strategies, Journal of Photochemistry and Photobiology C: Photochemistry Reviews. 24 (2015) 43–63. https://doi.org/10.1016/j.jphotochemrev.2015.06.002.
[15] M. Shamsipur, M.B. Gholivand, S. Dehdashtian, M. Feyzi, F. Jafari, Synthesis of Co/TiO_2 Nanocomposite and its Use in Construction of a Sensitive and Selective Sensor for Determination of Ciprofloxacin, AMR. 829 (2013) 563–567. https://doi.org/10.4028/www.scientific.net/AMR.829.563.
[16] X. Chen, A. Selloni, Introduction: Titanium Dioxide (TiO_2) Nanomaterials, Chemical Reviews. 114 (2014) 9281–9282. https://doi.org/10.1021/cr500422r.
[17] H. Li, J. Li, D. Chen, Y. Qiu, W. Wang, Dual-functional cubic cuprous oxide for non-enzymatic and oxygen-sensitive photoelectrochemical sensing of glucose, Sensors and Actuators B: Chemical. 220 (2015) 441–447. https://doi.org/10.1016/j.snb.2015.05.110.
[18] W. Zhan, Z. Chen, J. Hu, X. Chen, Vertical CuO nanowires array electrodes: Visible light sensitive photoelectrochemical biosensor of ethanol detection, Materials Science in Semiconductor Processing. 85 (2018) 90–97. https://doi.org/10.1016/j.mssp.2018.06.002.
[19] W.R. Siah, H.O. Lintang, M. Shamsuddin, H. Yoshida, L. Yuliati, Masking effect of copper oxides photodeposited on titanium dioxide: exploring UV, visible, and solar light activity, Catal. Sci. Technol. 6 (2016) 5079–5087. https://doi.org/10.1039/C6CY00074F.
[20] D.M. Tobaldi, L. Lajaunie, M. López-Haro, R. Ferreira, M. Leoni, M.P. Seabra, J. Calvino, L. Carlos, J.A. Labrincha, A Semiconducting Material Exhibiting Visible-Light Promoted Photochromism, Photoluminescent and Photocatalytic Activity, (2018). https://doi.org/10.26434/chemrxiv.7527572.v1.
[21] S. Luo, F. Su, C. Liu, J. Li, R. Liu, Y. Xiao, Y. Li, X. Liu, Q. Cai, A new method for fabricating a CuO/TiO2 nanotube arrays electrode and its application as a sensitive nonenzymatic glucose sensor, Talanta. 86 (2011) 157–163. https://doi.org/10.1016/j.talanta.2011.08.051.
[22] J. Chen, L. Xu, R. Xing, J. Song, H. Song, D. Liu, J. Zhou, Electrospun three-dimensional porous CuO/TiO2 hierarchical nanocomposites electrode for nonenzymatic glucose biosensing, Electrochemistry Communications. 20 (2012) 75–78. https://doi.org/10.1016/j.elecom.2012.01.032.
[23] Y. Cai, Y. Ye, S. Wu, J. Liu, C. Liang, Simultaneous Cu doping and growth of TiO2 nanocrystalline array film as a glucose biosensor, RSC Adv. 6 (2016) 78219–78224. https://doi.org/10.1039/C6RA15014D.
[24] J. Stanley, R.J. Sree, T. Ramachandran, T.G.S. Babu, B.G. Nair, Vertically Aligned TiO_2 Nanotube Arrays Decorated with CuO Mesoclusters for the Nonenzymatic Sensing of Glucose, J Nanosci Nanotechnol. 17 (2017) 2732–2739.
[25] D.M. Tobaldi, L. Lajaunie, A. Caetano, N. Rozman, M.P. Seabra, A. Sever Skapin, R. Arenal, J.A. Labrincha, Impact of Rutile Fraction on TiO2 Visible-Light Absorption and Visible-Light-Induced Photocatalytic Activity, (2018). https://doi.org/10.26434/chemrxiv.7461161.v1.
[26] A.C. Larson, R.B. Von Dreele, General Structure Analysis System (GSAS), Los Alamos National Laboratory Report LAUR, 2004.

[27] B.H. Toby, EXPGUI, a graphical user interface for GSAS, Journal of Applied Crystallography. 34 (2001) 210–213. https://doi.org/10.1107/S0021889801002242.
[28] P. Scardi, M. Ortolani, M. Leoni, WPPM: Microstructural Analysis beyond the Rietveld Method, Materials Science Forum. 651 (2010) 155–171. https://doi.org/10.4028/www.scientific.net/MSF.651.155.
[29] M. Leoni, T. Confente, P. Scardi, PM2K: a flexible program implementing Whole Powder Pattern Modelling, Zeitschrift Für Kristallographie Supplements. 23 (2006) 249–254. https://doi.org/10.1524/zksu.2006.suppl_23.249.
[30] D.M. Tobaldi, S.G. Leonardi, K. Movlaee, L. Lajaunie, M.P. Seabra, R. Arenal, G. Neri, J.A. Labrincha, Hybrid Noble-Metals/Metal-Oxide Bifunctional Nano-Heterostructure Displaying Outperforming Gas-Sensing and Photochromic Performances, ACS Omega. 3 (2018) 9846–9859. https://doi.org/10.1021/acsomega.8b01508.
[31] M. Karmaoui, A.B. Jorge, P.F. McMillan, A.E. Aliev, R.C. Pullar, J.A. Labrincha, D.M. Tobaldi, One-Step Synthesis, Structure, and Band Gap Properties of SnO2 Nanoparticles Made by a Low Temperature Nonaqueous Sol–Gel Technique, ACS Omega. 3 (2018) 13227–13238. https://doi.org/10.1021/acsomega.8b02122.
[32] R.G. Burns, Mineralogical Applications of Crystal Field Theory, Cambridge University Press, 1993.
[33] F.D.L. Peña, T. Ostasevicius, V.T. Fauske, P. Burdet, E. Prestat, P. Jokubauskas, M. Nord, K.E. MacArthur, M. Sarahan, D.N. Johnstone, J. Taillon, A. Eljarrat, V. Migunov, J. Caron, T. Furnival, S. Mazzucco, T. Aarholt, M. Walls, T. Slater, F. Winkler, B. Martineau, G. Donval, R. McLeod, E.R. Hoglund, I. Alxneit, I. Hjorth, T. Henninen, Luiz Fernando Zagonel, A. Garmannslund, 5ht2, Hyperspy V1.4, (2018). https://doi.org/10.5281/zenodo.1407391.
[34] L. Laffont, M.Y. Wu, F. Chevallier, P. Poizot, M. Morcrette, J.M. Tarascon, High resolution EELS of Cu–V oxides: Application to batteries materials, Micron. 37 (2006) 459–464. https://doi.org/10.1016/j.micron.2005.11.007.
[35] S. Bakardjieva, V. Stengl, L. Szatmary, J. Subrt, J. Lukac, N. Murafa, D. Niznansky, K. Cizek, J. Jirkovsky, N. Petrova, Transformation of brookite-type TiO2 nanocrystals to rutile: correlation between microstructure and photoactivity, J. Mater. Chem. 16 (2006) 1709–1716. https://doi.org/10.1039/B514632A.
[36] H. Zhang, J.F. Banfield, Thermodynamic analysis of phase stability of nanocrystalline titania, Journal of Materials Chemistry. 8 (1998) 2073–2076. https://doi.org/10.1039/a802619j.
[37] D.M. Tobaldi, N. Rozman, M. Leoni, M.P. Seabra, A.S. Škapin, R.C. Pullar, J.A. Labrincha, Cu–TiO_2 Hybrid Nanoparticles Exhibiting Tunable Photochromic Behavior, J. Phys. Chem. C. 119 (2015) 23658–23668. https://doi.org/10.1021/acs.jpcc.5b07160.
[38] F.C. Hawthorne, Mineralogical Society of America, eds., Spectroscopic methods in mineralogy and geology, Mineralogical Society of America, Washington, D.C., 1988.
[39] H. Irie, K. Kamiya, T. Shibanuma, S. Miura, D.A. Tryk, T. Yokoyama, K. Hashimoto, Visible Light-Sensitive Cu(II)-Grafted TiO_2 Photocatalysts: Activities and X-ray Absorption Fine Structure Analyses, The Journal of Physical Chemistry C. 113 (2009) 10761–10766. https://doi.org/10.1021/jp903063z.
[40] C. Ampelli, S.G. Leonardi, C. Genovese, P. Lanzafame, S. Perathoner, G. Centi, G. Neri, Monitoring of glucose in fermentation processes by using Au/TiO2 composites as novel modified electrodes, J Appl Electrochem. 45 (2015) 943–951. https://doi.org/10.1007/s10800-015-0874-4.
[41] S. Zhou, X. Feng, H. Shi, J. Chen, F. Zhang, W. Song, Direct growth of vertically aligned arrays of Cu(OH)2 nanotubes for the electrochemical sensing of glucose, Sensors and Actuators B: Chemical. 177 (2013) 445–452. https://doi.org/10.1016/j.snb.2012.11.035.
[42] J. Luo, S. Jiang, H. Zhang, J. Jiang, X. Liu, A novel non-enzymatic glucose sensor based on Cu nanoparticle modified graphene sheets electrode, Analytica Chimica Acta. 709 (2012) 47–53. https://doi.org/10.1016/j.aca.2011.10.025.

[43] H.-X. Wu, W.-M. Cao, Y. Li, G. Liu, Y. Wen, H.-F. Yang, S.-P. Yang, In situ growth of copper nanoparticles on multiwalled carbon nanotubes and their application as non-enzymatic glucose sensor materials, Electrochimica Acta. 55 (2010) 3734–3740. https://doi.org/10.1016/j.electacta.2010.02.017.
[44] L. Luo, L. Zhu, Z. Wang, Nonenzymatic amperometric determination of glucose by CuO nanocubes–graphene nanocomposite modified electrode, Bioelectrochemistry. 88 (2012) 156–163. https://doi.org/10.1016/j.bioelechem.2012.03.006.
[45] Z. Fan, B. Liu, X. Liu, Z. Li, H. Wang, S. Yang, J. Wang, A flexible and disposable hybrid electrode based on Cu nanowires modified graphene transparent electrode for non-enzymatic glucose sensor, Electrochimica Acta. 109 (2013) 602–608. https://doi.org/10.1016/j.electacta.2013.07.153.
[46] B. Yuan, C. Xu, L. Liu, Q. Zhang, S. Ji, L. Pi, D. Zhang, Q. Huo, Cu2O/NiOx/graphene oxide modified glassy carbon electrode for the enhanced electrochemical oxidation of reduced glutathione and nonenzyme glucose sensor, Electrochimica Acta. 104 (2013) 78–83. https://doi.org/10.1016/j.electacta.2013.04.073.
[47] J. Zhang, N. Ding, J. Cao, W. Wang, Z. Chen, In situ attachment of cupric oxide nanoparticles to mesoporous carbons for sensitive amperometric non-enzymatic sensing of glucose, Sensors and Actuators B: Chemical. 178 (2013) 125–131. https://doi.org/10.1016/j.snb.2012.12.070.
[48] X. Li, J. Yao, F. Liu, H. He, M. Zhou, N. Mao, P. Xiao, Y. Zhang, Nickel/Copper nanoparticles modified TiO2 nanotubes for non-enzymatic glucose biosensors, Sensors and Actuators B: Chemical. 181 (2013) 501–508. https://doi.org/10.1016/j.snb.2013.02.035.
[49] Y.-W. Hsu, T.-K. Hsu, C.-L. Sun, Y.-T. Nien, N.-W. Pu, M.-D. Ger, Synthesis of CuO/graphene nanocomposites for nonenzymatic electrochemical glucose biosensor applications, Electrochimica Acta. 82 (2012) 152–157. https://doi.org/10.1016/j.electacta.2012.03.094.